Published in "The European Physical Journal D 69(11): 1–11, 2015"
which should be cited to refer to this work.

Investigation of the intrinsic sensitivity of a ^{3}He/Cs magnetometer

Hans-Christian Koch[1,2,a], Georg Bison[3], Zoran D. Grujić[1], Werner Heil[2], Malgorzata Kasprzak[1,b], Paul Knowles[1,c], Andreas Kraft[2], Anatoly Pazgalev[5], Allard Schnabel[4], Jens Voigt[4], and Antoine Weis[1]

[1] Physics Department, University of Fribourg, 1700, Fribourg, Switzerland
[2] Department of Physics, Johannes Gutenberg-University, 55122 Mainz, Germany
[3] Paul Scherrer Institute, 5232 Villigen, Switzerland
[4] Physikalisch-Technische Bundesanstalt, 10587 Berlin, Germany
[5] Ioffe Physical Technical Institute, Russian Academy of Sciences, 194021 St. Petersburg, Russia

Abstract. We report on extensive studies on the intrinsic sensitivity of a combined ^{3}He/Cs magnetometer. The magnetometer relies on the detection of the free spin precession of nuclear spin polarized ^{3}He by optically pumped cesium magnetometers. We characterize the relevant processes involved in the detection and quantify their impact on the total sensitivity of the magnetometer. An expression is derived that predicts the sensitivity of this magnetometer scheme and the results are compared to experiments. Excellent agreement is found between theory and experiments, and implications for an application of a ^{3}He/Cs magnetometer in an experiment searching for a permanent neutron electric dipole moment are discussed.

1 Introduction

Many fundamental physics experiments require the precision knowledge and control of an applied magnetic field. The searches for permanent electric dipole moments (EDM) of elementary particles, atoms or molecules are among such experiments. A high precision experiment, currently conducted at Paul Scherrer Institute (PSI), Switzerland, searches for the existence of a neutron EDM (nEDM) [1]. The existence of a finite-valued nEDM is closely tied to long persisting questions of cosmology, such as the baryon asymmetry of the universe [2]. In the experiment the spin precession frequency of stored ultracold neutrons in homogeneous parallel and anti-parallel electric and magnetic fields is measured using Ramsey's technique of separated oscillatory fields [3]. A next generation nEDM experiment is currently being developed at PSI (n2EDM) and is expected to further constrain the value of the nEDM. In order to suppress and control systematic effects the experiment requires the precise measurement of an applied magnetic field of $\sim$1 μT and the tuning of field gradients. For this task we plan to integrate in the apparatus a ^{3}He magnetometer recording the free spin precession (FSP) frequency of nuclear spin polarized ^{3}He gas. During the FSP the ^{3}He magnetization precesses at the Larmor frequency

$$\omega_{\mathrm{L,He}} = |\boldsymbol{B}|\,\gamma_{\mathrm{He}} \tag{1}$$

which will be measured by detecting the associated rotating magnetic field with optically pumped Cesium magnetometers (CsOPMs). Compared to superconducting quantum interference devices, which are widely used to detect nuclear magnetic resonance, CsOPMs offer the advantage of operating at room temperature, thus easing the spatially-distributed positioning of a large number of individual sensors.

In a recent publication we have described the design and performance of a ^{3}He/Cs magnetometer prototype built to investigate this magnetometric scheme [4]. We have demonstrated that CsOPMs provide a convenient way to detect the ^{3}He FSP, permitting Cramér-Rao lower bound (CRLB) limited measurements of a 1 μT magnetic field that yield sensitivities as low as $\Delta B \sim 50$ fT with a 100 s integration time. In this paper we report on an extended study of the intrinsic sensitivity of the combined ^{3}He/Cs magnetometer concept. We have developed a semi-empirical formula which predicts the CRLB and shotnoise-limited magnetometric sensitivity of a ^{3}He/Cs magnetometer based on specific experimental parameters. The predictions are compared to experimental results obtained at the magnetically shielded room (BMSR-2) of Physikalisch Technische Bundesanstalt (PTB) in Berlin [5] and find excellent agreement with model estimations.

[a] e-mail: kochhc@googlemail.com
[b] *Present address:* Instituut voor Kern- en Stralingsfysica, Katholieke Universiteit Leuven, 3001 Leuven, Belgium
[c] *Present address:* LogrusData, Vienna, Austria

2 Magnetometer principle

The ^{3}He/Cs magnetometer concept is based on detecting (by CsOPMs) the weak rotating magnetic field accompanying the precessing of nuclear spin polarized ^{3}He atoms. The CsOPMs build on an optically-detected magnetic resonance effect. The sensor proper is an evacuated, paraffin-coated glass cell of 30 mm diameter that holds a droplet of cesium in an appendix which is connected to the main volume by a capillary to reduce depolarizing collisions of Cs vapor atoms with the bulk Cs [6]. The Cs vapor is optically pumped using circularly-polarized laser radiation resonant with the D1 transition, $\lambda \sim 895$ nm. The cell is enclosed in a pair of Helmholtz coils used to drive the magnetic resonance transitions by a weak rf field, $\boldsymbol{B}_{\rm rf}(t)$, oscillating at the Cs Larmor frequency $\omega_{\rm rf} \approx \omega_{\rm L,Cs}$ that is related to the modulus of the total magnetic field $\boldsymbol{B}$ via

$$\omega_{\rm L,Cs} = \gamma_{\rm Cs} \, |\boldsymbol{B}| \tag{2}$$

where $\gamma_{\rm Cs}/2\pi \approx 3.5$ kHz/μT is the cesium atom's gyromagnetic ratio. The magnetometers are operated in the so-called M_x configuration [7] with the rf field along the laser beam, $\hat{B}_{\rm rf} \parallel \hat{k}_{\rm Cs}$. The light power transmitted by the Cs cell is detected by a photodiode and the transimpedance amplified photocurrent signal demodulated by a lock-in amplifier referenced to $\omega_{\rm rf}$. Analytical expressions describing the lineshapes of the M_x magnetometer can be derived from the Bloch equations in the rotating wave approximation, yielding

$$S_R = \sqrt{S_{IP}^2 + S_{QU}^2} = \frac{G_0 \sqrt{\Gamma_2^2 + \delta\omega^2}\omega_1 \Gamma_1}{\sqrt{2}(2\Gamma_1(\Gamma_2^2 + \delta\omega^2) + \Gamma_2\omega_1^2)} \tag{3}$$

$$\tan\left(\frac{\pi}{2} + \phi\right) = \frac{S_{QU}}{S_{IP}} = -\frac{\delta\omega}{\Gamma_2} \tag{4}$$

for the amplitude (S_R)-phase (ϕ) parametrization of the demodulated signal [8]. Here, S_{IP} and S_{QU} denote the in-phase and quadrature components of the signal, respectively. G_0 is a saturation parameter that depends on the laser power and Γ_1, Γ_2 are the longitudinal and transverse relaxation rates of the Cs polarization, respectively. We have also introduced the detuning of the rf frequency from resonance

$$\delta\omega = \omega_{\rm L,Cs} - \omega_{\rm rf} \tag{5}$$

and expressed the rf field strength in terms of its associated Larmor frequency $\omega_1 = \gamma_{\rm Cs} B_{\rm rf}$.

The magnetic dipole field produced by a spherical volume of polarized ^{3}He at the magnetometer position $\boldsymbol{r}$ with respect to the sphere center is given by:

$$\boldsymbol{B}_{\rm He} = \frac{3\hat{r}(\hat{\mu}\cdot\hat{r}) - \hat{\mu}}{r^3} \frac{N_{\rm He} p \mu_{\rm He} \mu_0}{4\pi}. \tag{6}$$

Here p and $\mu_{\rm He}$ are the nuclear spin polarization and magnetic moment of the ^{3}He, while $\hat{\mu}$ represents the spatial orientation of the ^{3}He magnetization. Assuming a (room temperature) pressure of ~1 mbar, the ~70 mm diameter

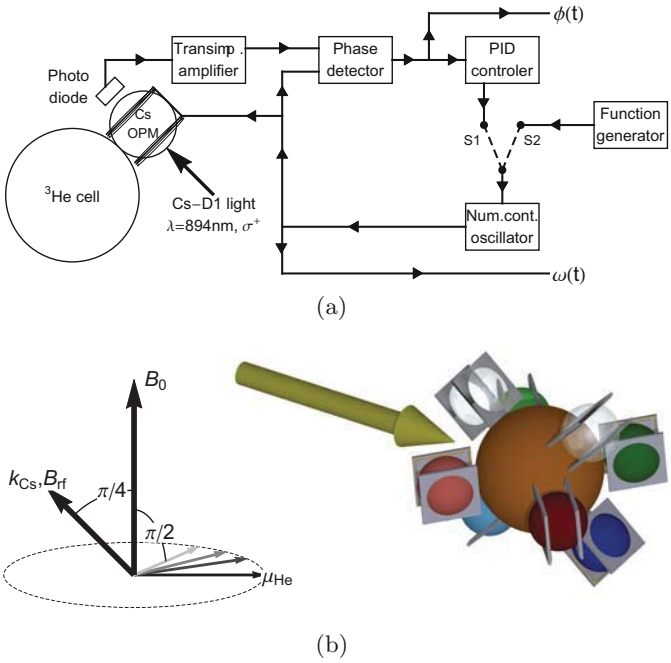

Fig. 1. (a) Schematic sketch of experiment and processing electronics. If the switch is set to position S1, the phase detector, PID controller and numerically controlled oscillator form a phase feedback loop and the CsOPM is operated in PS-mode. If set to S2 position the CsOPM can be operated in FF-mode (function generator supplies constant output) or frequency sweep measurements as shown in Figure 2 can be recorded (function generator supplies ramp). In the experiments described here, phase detector, PID controller, function generator and numerically controlled oscillator are all digitally implemented in a single device. (b) Left: geometry of the experiment. The ^{3}He magnetization $\boldsymbol{\mu}_{\rm He}$ is precessing in a plane perpendicular to $\boldsymbol{B}_0$, the $\boldsymbol{k}_{\rm Cs}$ of the CsOPM readout laser is at 45°. Right: geometry of the combined magnetometer. The large(orange) sphere in the center is the ^{3}He cell. The surrounding smaller spheres are the CsOPMs with the gray planes indicating the orientation of the printed circuit boards holding the individual rf coils. The (yellow) arrow denotes the direction of the B_0 field.

^{3}He cell contains $N_{\rm He} \approx 3\times10^{18}$ atoms following the ideal gas law. Evaluating equation (6) shows that the magnetic field of interest is on the order of pico-Tesla in the vicinity of the cell. In the experiments described in this work we have $B_0 \sim 1$ μT $\gg B_{\rm He}$, in which case equation (2) reduces to $\omega_{\rm L,Cs}(t) \propto |\boldsymbol{B}| = |\boldsymbol{B}_0 + \boldsymbol{B}_{\rm He}| \approx |\boldsymbol{B}_0| + \hat{B}_0 \cdot \boldsymbol{B}_{\rm He}(t)$. Under this condition the CsOPM is to first order only sensitive to the component of the ^{3}He field along $\boldsymbol{B}_0$. The precession of the ^{3}He magnetization can be expressed by a time dependent $\hat{\mu}(t)$ in equation (6). Assuming $\hat{B}_0 = \hat{z}$ and $\boldsymbol{\mu}$ rotating in an orthogonal plane (cf. Fig. 1b, left), the relevant component of the oscillating magnetic field is given by:

$$B_{\rm He,z} = \frac{N_{\rm He} p \mu_{\rm He} \mu_0}{4\pi r^3} 3\cos(\omega_{\rm L,He} t - \phi)\cos(\theta)\sin(\theta) \tag{7}$$

introducing standard spherical coordinates. The field component given by equation (7) will thus be maximized for $\theta = 45°$, so that the loci of optimal CsOPM positions are represented by two symmetric cones around $\hat{B}_0$ with tips centered at the ^{3}He cell center. The CsOPMs should thus be placed on these cones at a minimal distance $|\boldsymbol{r}|$ from the ^{3}He cell.

3 The experimental apparatus

The measurements presented below were performed in the magnetically shielded room BMSR-2 of Physikalisch Technische Bundesanstalt in Berlin using the combined ^{3}He/Cs magnetometer prototype described in detail in reference [4]. It consists of a 70 mm diameter spherical ^{3}He cell mounted in a structure that holds eight CsOPMs in the optimal detection geometry discussed above (cf. Fig. 1b, right). Nuclear spin polarization is created in the ^{3}He gas by metastable exchange optical pumping with 1.08 μm laser radiation traversing a plasma discharge in the ^{3}He cell. The maximal amplitude of the field oscillation created by the ^{3}He FSP that can be expected at the Cs cell centers can be calculated from equation (7). Inserting the dimensions of the ^{3}He cell (69–72 mm diameter, 2 mm wall thickness) and the CsOPMs (30 mm diameter) the calculation yields $\left|B_{\mathrm{He}}^{(\mathrm{max})}\right| = 34\ \mathrm{pT_{rms}}$. Each CsOPM has an individual rf coil pair. In order to avoid that the magnetic resonance in a given CsOPM is driven by the parasitic rf field from a neighboring sensor, an effect known as rf cross-talk, all magnetometers are driven at the same ω_{rf}.

Two different modes of operation were investigated, viz., the fixed-frequency mode (FF-mode) and the phase-stabilized mode (PS-mode). Figure 1a shows a schematic drawing of the data processing electronics for both modes of operation. In the FF-mode of operation the frequency ω_{rf} is kept constant, and magnetic field changes are detected via corresponding phase changes, following equation (4). If the magnetic field gradients are sufficiently small ω_{rf} can be chosen to have good overlap with the resonances of all CsOPMs and they can all be driven by the same rf. In the PS-mode of operation one CsOPM (master) is operated in a phase feedback loop. An error signal is derived from the phase difference between the magnetometer signal and the output of a numerically-controlled oscillator (NCO) that supplies the rf frequency for the CsOPM [9]. A PID controller minimizes this error signal by adjusting the frequency of the NCO. Under ideal conditions the CsOPM is thus always driven on resonance ω_{rf}=$\omega_{\mathrm{L,Cs}}$. This dynamically controlled ω_{rf} is then also used to drive the remaining CsOPMs (slaves). In the presence of (fluctuating) gradients this implies that the slaves are in general not driven exactly on resonance. Furthermore, due to the dependence of the ^{3}He FSP signal's phase on the relative position of the CsOPM (cf. Eq. (7)), the signals from the slaves will be qualitatively different and all depending on the master's performance. Such effects can be exploited in gradiometric measurements [10].

4 The measurement parameters

The sensitivity of the combined magnetometer depends on a set of parameters describing the properties of the optically detected magnetic resonance (ODMR) process in the CsOPM and the FSP of the ^{3}He gas. A detailed account of all effects affecting the CsOPM sensitivity is given in reference [6]. In the following we will separately address the most relevant effects and quantify their contribution to the total sensitivity.

4.1 Bandwidth limitation of CsOPM

As evidenced by the expressions describing the magnetometer signal lineshapes (Eqs. (3) and (4)), the CsOPM in M_x configuration can be considered as a driven harmonic oscillator with resonance frequency $\omega_{\mathrm{L,Cs}}$ periodically excitated at ω_{rf}. In general, the excitation frequency ω_{rf} is detuned from the resonance frequency $\omega_{\mathrm{L,Cs}}$ by an amount $\delta\omega$ given by equation (5). The detuning is affected both by variations of the magnetic field and of the excitation frequency. Following a change of the detuning, the ODMR process in the CsOPM undergoes a transient phase (and frequency) change during which the Cs spin precession adapts to the changed conditions. The settling time of this process depends on the lifetime τ=Γ_2^{-1} of the Cs polarization in the cell, where Γ_2 is the transverse spin relaxation rate. In perfect analogy with mechanical or electronic driven oscillators, the settling time can be related to the resonance's quality factor Q via

$$Q = \frac{\omega_{L,Cs}}{2\Gamma_2}. \tag{8}$$

Periodic changes of the detuning $\delta\omega \sim \cos(\omega_{\mathrm{mod}}t)$ are of particular interest for the present discussion. In that case, the settling process implies a frequency-dependent response of the system with a first-order low pass characteristic [11] $T_{\mathrm{Cs}}(f) = T^{(1)}(f)$, where

$$T^{(n)}(f) = \left[\frac{1}{1+(2\pi f\,\tau)^2}\right]^{n/2}, \tag{9}$$

is the generalized transfer function of an nth order filter. $T_{\mathrm{Cs}}(f)$ describes the response of the photodiode signal to a change of the detuning. The relaxation rate in the Cs cell will in general depend on different parameters, e.g., the quality of the coating, the size of the cell and the power of the resonant pump and readout light. It can be conveniently measured by recording the response of the magnetometer to a sweep of the rf frequency. The result of such a measurement is shown in Figure 2.

As described in Section 3, the CsOPMs can be operated in two different modes of operation. In the FF-mode, where ω_{rf} is being kept constant, any change of the detuning induced by a change of the magnetic field at the CsOPM's position will change the local Larmor frequency $\omega_{\mathrm{L,Cs}}$. The oscillating field produced by the ^{3}He-FSP introduces a periodic change of the detuning, and the frequency dependence of the CsOPM's response will be given

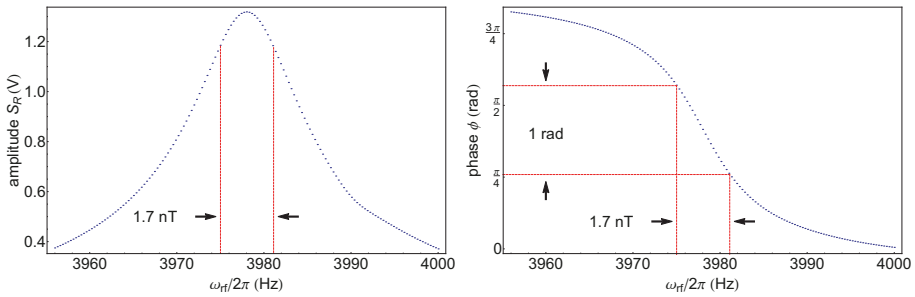

Fig. 2. S_R- and ϕ-signal of CsOPM when the rf frequency is tuned across the magnetic resonance. Graphs shown for $\Gamma_2/2\pi =$ 6.1 Hz, equivalent to 1.7 nT.

by the transfer function $T_{\mathrm{Cs}}^{(1)}(f)$. Since the typical lifetime of the Cs polarization in the paraffin coated cells is $\tau \sim 26$ ms, the low pass described by equation (9) has a -3dB cutoff frequency of typically $f_{\text{-3dB}} \approx 6$ Hz. This represents a severe bandwidth limitation for measurements performed in the FF-mode. An additional bandwidth limitation arises from the low-pass filter in the lock-in amplifier's demodulator used to extract the phase signal, an effect that can be characterized by a second transfer function, $T_{\mathrm{LIA}}(f)$. Assuming only small variations of the magnetic field $\gamma_{\mathrm{Cs}}\delta B \ll \Gamma_2$ and using equation (4) the response of the CsOPM's phase signal to a change of the magnetic field can be expressed as:

$$\delta\phi = \frac{\delta\omega}{\Gamma_2}\, T_{\mathrm{tot}} = \frac{\gamma_{\mathrm{Cs}}\,\delta B}{\Gamma_2}\, T_{\mathrm{tot}}, \tag{10}$$

where

$$T_{\mathrm{tot}} = T_{\mathrm{LIA}}\, T_{\mathrm{Cs}} \tag{11}$$

is the combined transfer function of the system caused by the two processes mentioned above. This assumption can be verified experimentally by measuring the response of the CsOPM to small periodic variations applied to the holding field B_0. The results of such a measurement in which the field modulation frequency f_{mod} is changed (at constant modulation amplitude) are shown in Figure 3. For each value of f_{mod}, the amplitude $\delta\phi$ of the corresponding phase oscillation was inferred from the FFT spectrum of the time dependent phase signal. The experimental results are in excellent agreement with the theoretical predictions.

In the PS-mode of operation the phase-stabilized loop dynamically readjusts ω_{rf} to track changes of the Larmor frequency. In the ideal case one has $\omega_{\mathrm{L,Cs}} = \omega_{\mathrm{rf}}$ at all times, so that the CsOPM is always driven at resonance and no change of detuning occurs. In this mode of operation, the CsOPM is free from the bandwidth limitation imposed by the 'free-running' FF-mode. In reality the bandwidth is limited by the frequency characteristics of the feedback loop whose bandwidth, however, can be considerably larger than the one imposed by $T_{\mathrm{LIA}}T_{\mathrm{Cs}}$ under free-running conditions. In Section 7 implications for the magnetometric sensitivity in this mode of operation will be discussed.

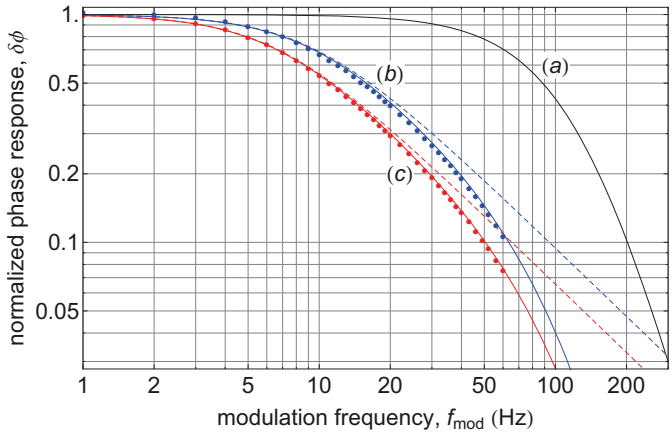

Fig. 3. Experimental and theoretical frequency response of two CsOPMs driven in FF-mode. (a) Transfer function $T_{LIA} = T^{(4)}$ of the used 4th order (-24 dB/oct) lock-in amplifier demodulation filter calculated according to equation (9) with $\tau = 1.16$ ms. (b,c) dashed lines: Transfer functions T_{Cs}=$T^{(1)}$ of two CsOPMs, corresponding to a 1st order filter with $\tau = 1/\Gamma_{Cs}$. The lifetimes are $\tau \approx 17$ ms for the blue curve and $\tau \approx 24$ ms for the red curve, respectively. (b,c) Solid lines: Combined transfer functions $T_{LIA}T_{Cs}$ for the two CsOPMs. The dots represent experimentally measured points.

4.2 Sensitivity loss due to permanent detuning

An additional effect has to be considered when operating multiple CsOPMs at an identical fixed frequency. Due to unavoidable inhomogeneities of the magnetic field, the Larmor frequencies of the individual CsOPMs will in general differ $\omega_{\mathrm{L,Cs}}^{(i)} \neq \omega_{\mathrm{L,Cs}}^{(j)}$. This results in some, or all CsOPMs being effectively driven at a finite detuning, even in a perfectly stable field. We consider two effects that are caused by such a permanent detuning. On one hand, the spread of Larmor frequencies will reduce the amplitude $a_{Cs}(\delta\omega)$ of the demodulated signal. On the other hand, the spread will affect the effective slope of the phase curve. Both effects can be experimentally quantified by measurements of the frequency sweep response functions, such as shown in Figure 2. Based on equation (4), the off-resonance value of the phase slope for a constant detuning

$\delta\omega'$ is given by:

$$m(\delta\omega')=\left.\frac{\partial\phi}{\partial\delta\omega}\right|_{\delta\omega'}=\frac{\partial}{\partial\delta\omega}\arctan\left(\frac{-\Gamma_2}{\delta\omega}\right)\Bigg|_{\delta\omega'}=\frac{\Gamma_2}{\Gamma_2^2+\delta\omega'^2}. \tag{12}$$

The on-resonance slope $m(\delta\omega'=0)=1/\Gamma_2$ will be reduced for detunings $\delta\omega'\neq 0$. A permanently detuned CsOPM will thus produce a smaller response signal to a given magnetic perturbation. The response reduction is given by:

$$\epsilon_\phi(\delta\omega')=\frac{m(\delta\omega')}{m(\delta\omega'=0)}=\frac{\Gamma_2^2}{\Gamma_2^2+\delta\omega'^2}. \tag{13}$$

As noted above, the amplitude S_R also depends on the detuning and will be maximal for $\delta\omega=0$. The consequences for the signal/noise ratio arising from this will be discussed in Section 5.

5 Signal to noise ratio and sensitivity

Even under optimal experimental conditions the magnetometer signal will exhibit a fundamental noise level caused by processes inherent to the detection mechanism. The most prominent of such processes is the photocurrent shotnoise (PSN), a fluctuation of the current produced by the photodiode due to the corpuscular nature of light and electric current. Since the relatively weak ($I_{\mathrm{AC}}<0.1\ \mu$A) oscillatory current carrying the magnetometric information is superimposed on a much larger ($I_{\mathrm{DC}}\sim 3\ \mu$A) DC current, it is reasonable to assume that the PSN is dominated by fluctuations of I_{DC}, whose spectral density is given by:

$$\rho_{\mathrm{I,PSN}}=\sqrt{2\,e\,I_{\mathrm{DC}}}, \tag{14}$$

where e is the elementary charge. Other sources of noise, such as fluctuations of the magnetic field (magnetic field noise, MN) or electronic pick-up by the signal cables that may be present will add quadratically to this fundamental noise floor. The optimal case, in which the PSN is the only source of noise is referred to as the shotnoise limit.

It is important to understand that different noise processes, such as the PSN and MN affect the phase signal in qualitatively different manners. Let us first consider the case of purely magnetic field noise. MN affects the magnetic resonance process and its effect on the phase signal – evaluated using equation (10) – is subject to the bandwidth-limiting atomic filtering of the magnetic resonance process. Since the signal of interest (magnetic field oscillation) and the signal noise (magnetic field fluctuations) are equally bandwidth limited, e.g., undergo the same filtering by T_{tot}, the signal to noise-density ratio (SNDR) is independent of this bandwidth limitation. This independence also holds under the assumption of a permanently detuned magnetometer, as introduced in Section 4.2. In order to illustrate this we consider a periodic magnetic field fluctuation, e.g., the oscillating field $\delta B=b_{\mathrm{He}}$ created by the ^{3}He-FSP at the position of the CsOPM and assume a Gaussian magnetic noise spectral density ρ_{B}. The $SNDR_B$ for the magnetic quantities and the $SNDR_\phi$ on the phase signal are

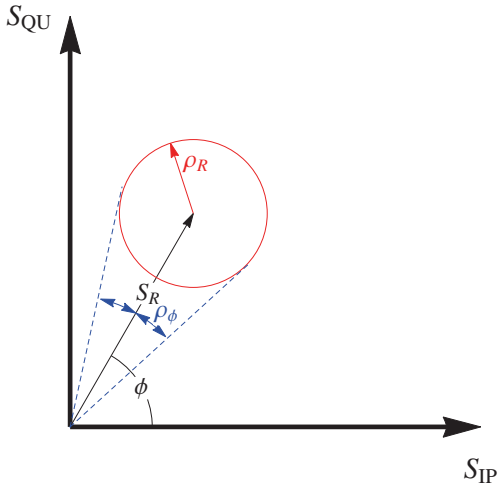

Fig. 4. Phasor plot of a signal with amplitude S_R and phase ϕ affected by Gaussian amplitude noise. The noise densities on the in-phase (S_{IP}) and quadrature (S_{QU}) components are statistically independent and of equal magnitude. They can thus be visualized by a circle, and it follows that $\rho_R=\sqrt{\rho_{IP}^2+\rho_{QU}^2}$. The root power spectral density of the corresponding phase noise $\rho_\phi=\rho_R/S_R$ follows from simple geometrical considerations.

$$SNDR_B=\frac{b_{\mathrm{He}}}{\rho_{\mathrm{B}}}=\frac{\delta\phi}{\rho_\phi}=SNDR_\phi. \tag{15}$$

A different situation occurs with PSN-produced signal fluctuations. This case is particularly interesting since it is often encountered with magnetically well shielded experimental conditions where the PSN is by far the dominant noise process of the measurement. Starting from equation (14) we can calculate the impact of the PSN on the phase signal. We first consider that the photodiode current is converted to a voltage signal by a transimpedance amplifier (TA) with frequency dependent gain $g_{V/A}(f)$. Since the lock-in amplifier in the subsequent step of the processing chain extracts only the signal close to the reference frequency $\omega_{\mathrm{rf}}\approx\omega_{\mathrm{L,Cs}}$, and assuming again that the noise is mainly caused by the fluctuating DC component of the photocurrent we can approximate the voltage noise spectral density after the TA as:

$$\rho_{\mathrm{V,PSN}}=\rho_{\mathrm{I,PSN}}g_{V/A}(\omega_{\mathrm{L,Cs}})=\rho_{\mathrm{I,PSN}}g_{\mathrm{AC}}. \tag{16}$$

Here we have defined $g_{V/A}(\omega_{\mathrm{L,Cs}})=g_{\mathrm{AC}}=2.53\times10^7$ V/A as the AC gain of the TA at the Cs Larmor frequency. The PSN will thus translate into noise of the in-phase and quadrature components of the lock-in detection process, so that the resulting effect on the phase signal can be deduced from Figure 4 to be given by:

$$\rho_{\phi,PSN}=\frac{\rho_{\mathrm{V,PSN}}}{S_R}, \tag{17}$$

where $S_R = \sqrt{S_{IP}^2 + S_{QU}^2}$ is the (detuning-dependent) amplitude of the lock-in signal. One can define a noise equivalent magnetic field NEM, i.e., the magnetic field fluctuation that leads to a signal noise identical to the PSN, by scaling the phase noise to magnetic field units. Using equation (10) one finds

$$NEM = \rho_{B,PSN} = \frac{\rho_{\phi,PSN}\,\Gamma_2}{\gamma_{\mathrm{Cs}}} = \frac{\rho_{\mathrm{I,PSN}}\,g_{\mathrm{AC}}\,\Gamma_2}{S_R\,\gamma_{\mathrm{Cs}}}. \quad (18)$$

We now discuss the implications for the SNDR assuming a ^{3}He-FSP signal b_{He} which is detected by a CsOPM in the shotnoise limit. Due to the filtering processes introduced above, the CsOPM will effectively detect a smaller oscillation amplitude

$$b'_{\mathrm{He}} = T_{\mathrm{tot}}(\omega_{\mathrm{L,He}})\,b_{\mathrm{He}}. \quad (19)$$

The NEM, on the other hand, is only subject to the LIA filter, so that

$$\rho'_{B,PSN} = \rho_{B,PSN} T_{\mathrm{LIA}}. \quad (20)$$

Combining the last two equations we find for the effective SNDR

$$SNDR' = \frac{b'_{\mathrm{He}}}{\rho'_{B,PSN}} = \frac{T_{Cs}(f_{\mathrm{He}})\,T_{LIA}(f_{\mathrm{He}})\,b_{\mathrm{He}}}{T_{LIA}(f_{\mathrm{He}})\,\rho_{B,PSN}} \quad (21)$$

$$= \frac{a_{Cs}\,\gamma_{Cs}\,b_{\mathrm{He}}}{\rho_{V,PSN}\sqrt{\Gamma_2^2 + \omega_{\mathrm{He}}^2}}, \quad (22)$$

where we used equations (9) and (18) in the last line. The important conclusion of equation (22) is that in the shotnoise limit the SNDR depends on the linewidth of the CsOPM and the frequency of the signal to be measured.

The considerations presented so far were restricted to a CsOPM with a zero permanent detuning. We will now address the case $\delta\omega' \neq 0$. Equation (13) describes the dependence of the phase response to magnetic perturbations in that case. If we consider again a situation in which the dominant measurement noise is the PSN, we find that – due to the reduced value of S_R – the resulting phase noise of the detuned magnetometer will be larger than the corresponding noise in the $\delta\omega = 0$ case. Replacing S_R by $a'_{Cs}(\delta\omega')$ in equation (17) we can relate the phase noise of the detuned CsOPM to the PSN, and the ratio of the noise densities for both cases is found to be

$$\epsilon_\rho(\delta\omega) = \frac{\rho'_\phi}{\rho_\phi} = \frac{a_{Cs}(\delta\omega = 0)}{a'_{Cs}(\delta\omega')}. \quad (23)$$

The effect of the permanent detuning can thus be expressed by the factor

$$c(Cs_i) = \frac{\epsilon_\phi(Cs_i)}{\epsilon_\rho(Cs_i)} \quad (24)$$

for each individual CsOPM. Figure 5 shows a plot of this factor for a CsOPM under real measurement conditions. It can be seen that the effect stays negligibly small for small detunings but becomes considerable when the detuning approaches the linewidth of the CsOPM.

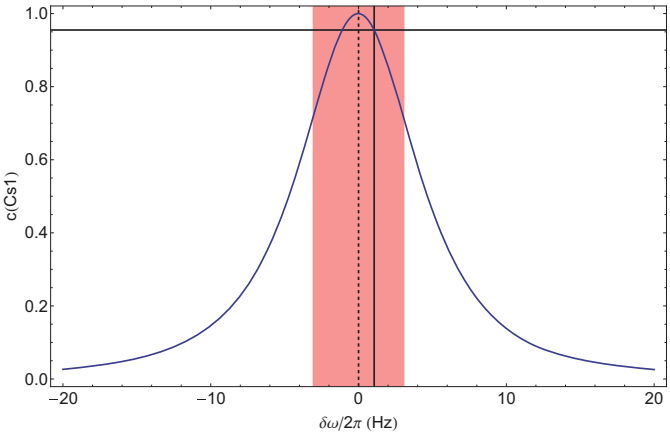

Fig. 5. Plot of $c(Cs_1) = \epsilon_\phi(Cs_1)/\epsilon_\rho(Cs_)$. The values were obtained as described in the text. The shaded red vertical band illustrates the linewidth $\Gamma_2/2\pi = 6.1$ Hz of this magnetometer. The solid vertical line denotes the actual detuning $\delta\omega'/2\pi = 1.06$ Hz of the CsOPM during operation, leading to a sensitivity reduction by $c = 0.96$ as indicated by the horizontal line.

Finally, we combine the effects of bandwidth limitation and permanent detuning to derive the following expression for the detection SNDR

$$\mathrm{SNDR}'' = \mathrm{SNDR}'\frac{\epsilon_\rho}{\epsilon_\phi} = \frac{a_{Cs}\,b_{\mathrm{He}}\gamma_{Cs}}{\rho_{V,PSN}\sqrt{\Gamma_2^2 + \omega_{\mathrm{He}}^2}}\frac{\epsilon_\rho}{\epsilon_\phi}. \quad (25)$$

6 Sensitivity of the combined magnetometer

Using the results derived above we are now able to predict the sensitivity of a ^{3}He/Cs magnetometer consisting of a ^{3}He cell and a single CsOPM. The precision with which the magnetic field can be determined depends on the precision with which the average frequency of the ^{3}He FSP can be measured in a given integration time T_M. Information theory sets a fundamental limit to this precision, the so called Cramér-Rao lower bound (CRLB) [12,13], which states that the variance of frequency estimation from a discrete-sample signal [14] is bound to obey

$$\sigma_{\mathrm{f}}^2 \geq \frac{6}{(2\pi)^2\,\mathrm{SNDR}^2\,T_M^3}, \quad (26)$$

which implies

$$\sigma_{\mathrm{B}}^2 \geq \frac{6}{\mathrm{SNDR}^2\,T_M^3\gamma_{\mathrm{He}}^2}. \quad (27)$$

for the measurement of the magnetic field.

We note that in general we are dealing with a slightly more complicated situation because the amplitude of the ^{3}He-FSP signal decays over time due to relaxation. This is taken into account by introducing an additional factor $C \geq 1$ in equations (26) and (27) that takes the damping

into account [15]. However, under homogeneous magnetic field conditions, the ^{3}He polarization decays very slowly so that for sufficiently short measurement times $T_M \ll \Gamma^{-1}$ the FSP amplitude can be considered constant, so that $C \approx 1$. For the measurements presented in the following section the decay time of ^{3}He was $\Gamma^{-1} \sim 13\,000$ s which allows this simplified treatment for measurement times up to several hundreds of seconds. Following the notation in reference [4], we parametrize the performance of the combined magnetometer by a sensitivity parameter η which absorbs the SNDR dependence of the detection,

$$\eta = \sigma_B T_M^{3/2} = \frac{\sqrt{6}}{\mathrm{SNDR}\,\gamma_{\mathrm{He}}}. \tag{28}$$

Evaluating this expression for the effective SNDR of each individual CsOPM yields a corresponding (sensor-specific) sensitivity parameter.

As a last step we assume the effects of a partially polarized ^{3}He sample, or an imperfect $\pi/2$ spin-flip. Both imperfections lead to a decrease of the FSP amplitude according to

$$b_{\mathrm{eff}} = p\,\sin(\theta_{\mathrm{flip}})\,b_{\mathrm{max,He}} = p_{\mathrm{eff}}\,b_{\mathrm{max,He}} \tag{29}$$

where we have introduced an effective polarization $p_{\mathrm{eff}} \leq 1$. Merging the results of equations (25), (28) and (29) we find

$$\eta_B^{theor} = \frac{\sqrt{6}\,\rho_{V,PSN}\,\sqrt{\Gamma_2^2 + \omega_{\mathrm{He}}^2}(\Gamma_2^2 + \delta\omega'^2)}{a'_{Cs}(\delta\omega')\,\Gamma_2^2\,p_{\mathrm{eff}}\,b_{\mathrm{max,He}}\,\gamma_{\mathrm{He}}\,\gamma_{Cs}}. \tag{30}$$

7 CsOPMs driven in PS mode

As we have seen, the FF-mode of operation, although very convenient and transparent, introduces a severe bandwidth limitation. This degrades the performance of the combined magnetometer at high fields in conditions where the PSN is the dominant noise source. In the PS-mode the measurement bandwidth is defined by the characteristics of the feedback loop [11]. In this mode of operation much higher bandwidths can be achieved which will lead to increased amplitudes of the ^{3}He oscillation in the measurement signal. The question arises if this goes hand in hand with an increase of SNDR and thus improved sensitivities can be expected in this mode of operation.

Let us assume a constant magnetic field B_0 and loop adjusted such that the CsOPM's phase is $\phi = 0$ on resonance $\omega_{\mathrm{rf}} = \omega_{\mathrm{L,Cs}} = \gamma_{\mathrm{Cs}} B_0$. A change of the magnetic field δB leads to a change of the CsOPMs phase $\delta\phi = \frac{\delta B \gamma_{\mathrm{Cs}}}{\Gamma_2}$ (in the absence of any bandwidth limitations). The loop reacts to this phase change by an adjustment of the loop frequency $\delta\omega_{\mathrm{PS}}$ thereby minimizing the error signal

$$\delta\phi_{\mathrm{PS}} = \delta\phi - \frac{\delta\omega_{\mathrm{PS}}}{\Gamma_2}. \tag{31}$$

In case of the ^{3}He FSP detection we deal with a periodic magnetic perturbation at frequency f. The minimization will only work properly if the feedback loop's bandwidth f_{BW} is larger than the oscillation frequency $f_{\mathrm{BW}} \gg f$. Even at sufficient bandwidth, a finite phase error (error signal) $\delta\phi_{\mathrm{PS}}$ is maintained the magnitude of which depends on the gain characteristics of the loop via

$$\delta\omega_{\mathrm{PS}} = \delta\phi_{\mathrm{PS}}\kappa(f), \tag{32}$$

where $\kappa(f)$ is a gain factor at the oscillation frequency f. From equation (31) we see that for a properly working feedback loop the full magnetic oscillation amplitude is given by:

$$\delta B = \frac{\Gamma_2\delta\phi_{\mathrm{PS}} + \delta\omega_{\mathrm{PS}}}{\gamma_{\mathrm{Cs}}}. \tag{33}$$

Combining this with equation (32), we obtain

$$\delta B = \frac{\delta\omega_{\mathrm{PS}}}{\gamma_{\mathrm{Cs}}}\left(\frac{\Gamma_2}{\kappa(f)} + 1\right). \tag{34}$$

To investigate the achievable SNDR in the PS mode we again have to make a separate case for the PSN which causes fluctuations of the CsOPM's phase signal that are not related to magnetic field fluctuations. The feedback loop will equally react to these fluctuations by adjustments of the drive frequency $\omega_{\mathrm{rf}} = \widetilde{\omega}_{\mathrm{PS}}$ thereby actually detuning the CsOPM from resonance, $\widetilde{\omega}_{\mathrm{PS}} \neq \omega_{\mathrm{L,Cs}}$. As a result the response of the magnetometer to these adjustments of the drive frequency becomes again bandwidth limited by the lifetime of the Cs polarization. We can express this detuning in magnetic units by a relation similar to equation (33),

$$\delta\widetilde{B} = \frac{\Gamma_2\delta\phi_{\mathrm{PS}} + T_{\mathrm{Cs}}(f)\delta\widetilde{\omega}_{\mathrm{PS}}}{\gamma_{\mathrm{Cs}}} = \frac{\delta\widetilde{\omega}_{\mathrm{PS}}}{\gamma_{\mathrm{Cs}}}\left(\frac{\Gamma_2}{\kappa(f)} + T_{\mathrm{Cs}}(f)\right), \tag{35}$$

where in the last step equation (32) was used. We assume now a measurement signal originating from an oscillating magnetic field, e.g., the ^{3}He FSP $\delta B = b_{\mathrm{He}}$ and signal noise being caused by PSN $\delta\widetilde{B} = \rho_{\mathrm{B,PSN}} = \mathrm{NEM}$. The SNDR of the loop frequency signal can be written as

$$\mathrm{SNDR}_{\mathrm{PS}} = \frac{\delta\omega_{\mathrm{PS}}}{\delta\widetilde{\omega}_{\mathrm{PS}}} = \frac{\delta B}{\delta\widetilde{B}}\,\frac{T_{\mathrm{Cs}}(f) + \Gamma_2/\kappa(f)}{1 + \Gamma_2/\kappa(f)} \tag{36}$$

$$= \frac{b_{\mathrm{He}}}{\rho_{\mathrm{B,PSN}}} \times \frac{T_{\mathrm{Cs}}(f) + \Gamma_2/\kappa(f)}{1 + \Gamma_2/\kappa(f)}. \tag{37}$$

Inspection of equation (37) in the high gain limit ($\kappa(f) \gg \Gamma_2$) shows that the maximum achievable SNDR is

$$\lim_{\kappa\to\infty} \mathrm{SNDR}_{\mathrm{PS}} = \frac{b_{\mathrm{He}}}{\rho_{\mathrm{B,PSN}}} T_{\mathrm{Cs}}(f), \tag{38}$$

which is equal to the SNDR for a CsOPM with zero permanent detuning driven in FF-mode derived in equation (21). The frequency dependence of the SNDR in both modes of operation is thus identical.

Finally we visualize the frequency dependence of the sensitivity (for both modes of CsOPM operation) by a plot of η as a function of the signal frequency. We assume a CsOPM with given linewidth and NEM driven at

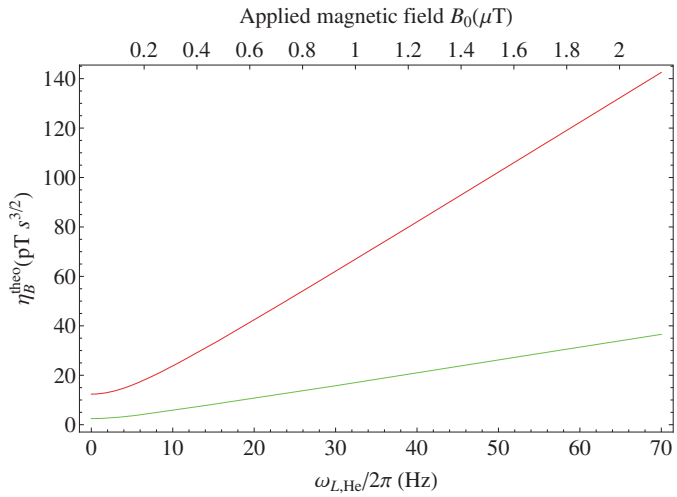

Fig. 6. Dependence of the magnetometric sensitivity on the frequency of the FSP signal, e.g., the magnitude of the holding field. The upper (red) curve corresponds to parameters obtained for Cs1 during the measurements presented here. The lower curve assumes the parameters of the best Cs cell reported in reference [6] ($\Gamma_2/2\pi$ = 4.75 Hz, NEM = 7 fT/$\sqrt{\text{Hz}}$). Both cases assume $|B_{\text{He}}^{(\max)}|$ = 34 pT_{rms}, see text for details.

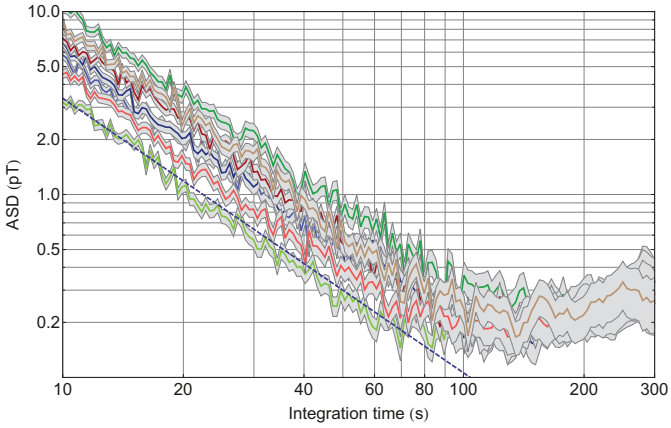

Fig. 7. ASDs of seven CsOPMs simultaneously detecting the ^{3}He-FSP. The gray regions around the curves represent the 1σ confidence band. The relative vertical position of the individual curves depends on the individual SNDR. For short integration times the characteristic $T_M^{-3/2}$ dependence for a CRLB-limited estimation is visible. For longer times the ASD becomes limited by the stability of the applied magnetic field. For the lowest curve the fit by equation (41) is also shown.

zero permanent detuning. We further assume a 100% polarized cell and ideal spin flip, meaning a maximal FSP amplitude $\left|B_{\text{He}}^{(\max)}\right|$ = 34 pT_{rms} (cf. Sect. 3). Under these assumptions equation (30) reduces to

$$\eta_B^{theo} = \text{NEM}\frac{\sqrt{6}\sqrt{\Gamma_2^2+\omega_{L,\text{He}}^2}}{\gamma_{\text{He}}\Gamma_2\left|B_{\text{He}}^{(\max)}\right|}. \tag{39}$$

A plot of this function for two different Cs cells is shown in Figure 6, see figure caption for details.

8 Measurements

We have checked the validity of equation (30) by comparing the predicted sensitivity parameters to experimental values. The experimental sensitivity parameters were obtained by recording simultaneously the phase signals of all CsOPMs detecting the ^{3}He-FSP. The CsOPMs were driven in the FF-mode of operation at a common frequency chosen to have good overlap with the magnetic resonances in all individual sensors. In an offline analysis, a sinusoidal function

$$s(t) = a_0 + a\cos(\omega_{\text{L,He}}t - \phi_0) \tag{40}$$

was fit to the data in order to extract the FSP frequency $\omega_{\text{L,He}}$. The Allan standard deviations (ASD) [16] of the resulting seven frequency estimates (the signals from one of the sensors could not be used because of DAQ problems) are shown in Figure 7. As expected for a CRLB limited estimation process they exhibit the characteristic $T_M^{-3/2}$ dependence for short integration times $T_M < 100$ s while for longer times the ASD grows due to instabilities of the magnetic field. A function

$$ASD = \eta_B^{meas}T_M^{-3/2} \tag{41}$$

was fit to the CRLB limited part of the data shown in Figure 7 to extract the experimental sensitivity parameter η_B^{meas}, the fitted function is shown for the lowest-lying curve. The results of these fits are summarized in Table 1 together with the theoretically predicted values derived by equation (30). The effective polarization which enters in the calculations of the η_B^{theo} was calculated from independent measurements of p and θ_{flip}. Details of the θ_{flip} measurement can be found in reference [8] and will be published in a later paper. The flipping angle was found to be $\theta_{\text{flip}} = 68.0(6)°$. The determination of the spin polarization has to be taken with some caution since it is based on comparing the measured FSP amplitudes to theoretical expectations. This requires a precise knowledge of the pressure and size of the sample cell. The amplitudes may also be affected by mechanical imperfections such as slightly different distances of the CsOPMs from the ^{3}He cell due to imperfect sphericity. The calculation assumes furthermore the validity of the bandwidth- and detuning-dependent CsOPM responses presented in Sections 4.2 and 4.1. The procedure yields $p = 0.71(6)$ where the large error is caused by the mechanical imperfections mainly. This is also the major cause for the rather large error on η_B^{theo} in Table 1.

An additional systematic uncertainty is connected to the measurement of the PSN through I_{DC}. Although this was done rather shortly before the measurements which went into the analysis of the sensitivity, it can not be excluded that the actual light power of each sensor was

Table 1. Measured and predicted sensitivity parameters η_B for different CsOPMs. The sensor Cs7 suffered from a DAQ problem and produced no reliable signals. The large errors on the predicted values are due to the uncertainty of the degree of polarization. Note that Cs2 and Cs7 were handled by a different DAQ system and are thus not directly comparable.

CsOPM	η_B^{theo}(pT · s$^{3/2}$)	η_B^{meas}(pT · s$^{3/2}$)
Cs1	118(11)	106(1)
Cs8	313(28)	324(2)
Cs4	161(15)	175(1)
Cs5	196(18)	196(2)
Cs6	241(22)	226(2)
Cs3	156(14)	147(1)
Cs2	181(17)	258(2)
Cs7	254(23)	–

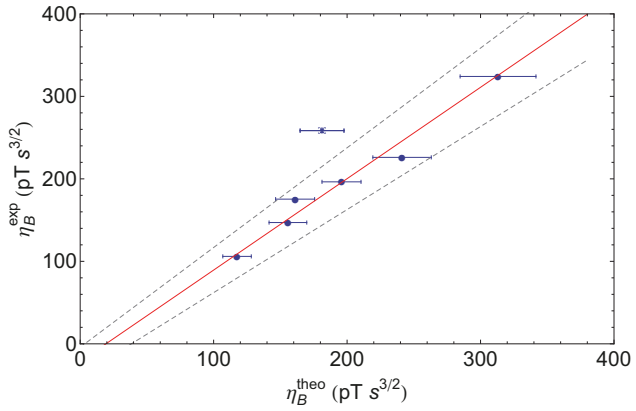

Fig. 8. Measured versus predicted sensitivity parameters. The dependence is given by $\eta_B^{meas} = 1.11(10)\eta_B^{theo} - 21.4(17.3)$ pT s$^{3/2}$. The vertical errors are too small to be visible. The data point depicted by the open square belongs to Cs2. Since this CsOPM was handled on a different DAQ system, this point was not included in the analysis.

slightly different during data taking due to a drift of the laser output power.

The predicted and measured sensitivities are plotted against each other in Figure 8. A linear regression was performed to extract the dependence. It can be seen that the predictions agree with the measured values within the uncertainties of the measurement. We thus conclude that equation (30) adequately describes the sensitivity in the FF-mode of operation and that our measurements were indeed shotnoise- and CRLB-limited since equation (30) predicts the sensitivity under these assumptions.

9 Implications for the n2EDM experiment

As discussed in reference [4] and elsewhere [17] the current design of the n2EDM experiment foresees two large, flat cylindrical ^{3}He magnetometer cells installed symmetrically above and below the cylindrical neutron precession chambers. In the experiment a homogeneous magnetic field $B_0 \approx 1$ μT will be applied along the cylinder

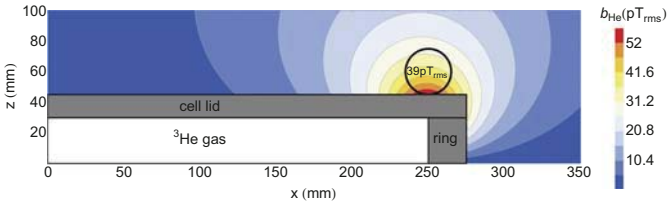

Fig. 9. Simulation of the ^{3}He FSP amplitude for a possible n2EDM geometry as a function of the CsOPM position, only one quadrant is shown. A cylindrical ^{3}He cell of inner height 60 mm and radius 250 mm filled with 100 % polarized gas at 1 mbar was assumed. The cell walls are denoted by the filled gray region, the black circle identifies the optimal position for a CsOPM.

axis $\hat{z}$. Based on our studies we can estimate the achievable sensitivity of a ^{3}He/Cs magnetometer in the n2EDM experiment at PSI. Since design details are still under discussion, we make some reasonable assumptions about a likely geometry. For safety reasons the ^{3}He cells have to withstand the large forces that may arise in case the magnetometer is to be operated in atmospheric pressure. We chose a cylindrical cell of 60 mm inner height and 250 mm radius filled with 100% polarized ^{3}He gas at 1 mbar for the example in Figure 9. The cells will be made from borosilicate glass and consist of a ring of radial width 25 mm and height 60 mm and two lid plates of thickness 15 mm. Figure 9 visualizes the results of a simulation in terms of a contour plot of the ^{3}He FSP amplitude in the $\hat{x}$-$\hat{z}$ plane (the ^{3}He magnetization is precessing in the $\hat{x}$-$\hat{y}$ plane). It can be seen that in this geometry a maximum ^{3}He FSP amplitude of $B_{\mathrm{He}}^{\mathrm{max,n2EDM}} = 39$ pT$_{\mathrm{rms}}$ can be expected which compares well to the $B_{\mathrm{He}}^{\mathrm{max,proto}} = 34$ pT$_{\mathrm{rms}}$ found for the prototype magnetometer. We can thus estimate the ultimate achievable magnetometric sensitivity per CsOPM in the n2EDM experiment by scaling the values from Figure 6 by $B_{\mathrm{He}}^{\mathrm{max,proto}}/B_{\mathrm{He}}^{\mathrm{max,n2EDM}} \approx 0.87$. Considering typical neutron storage times used in the current nEDM experiment this translates into a statistical measurement uncertainty of $\Delta B \approx 16$ fT in 100 s ($\Delta B \approx 6$ fT @ 200 s) measurement time per CsOPM. Because of the large size of the ^{3}He cell a large number ($N_{\mathrm{Cs}} > 25$) of readout CsOPMs can be envisioned. The error of the simultaneous measurement of the ^{3}He Larmor Frequency by all these CsOPMs will scale as $N_{\mathrm{Cs}}^{-1/2}$ as was shown in reference [4].

In addition, the magnetic field readings of the two ^{3}He magnetometer cells will yield information about magnetic field gradients which represent a major cause of systematic errors in the nEDM measurement [18]. While the measurement of longitudinal gradients $\partial B_0/\partial z$ is straightforward, the combined magnetometer will also give a potential access to transverse gradients $\partial B_0/\partial r$. The ^{3}He will be nuclear spin polarized and filled into the cells by a dedicated external compressor unit [19]. Since this technique allows to fill the ^{3}He cells at different pressures, the magnetometer can be operated in different dynamic regimes. Exploiting the pressure- and gradient-dependence of the volume

averaged Larmor frequency change $\Delta\Omega_0$ investigated by Cates et al. [20],

$$\Delta\Omega_0 \approx \frac{R_{cell}^2}{10\Omega_0}\left(|\nabla\Omega_{1,x}|^2 + |\nabla\Omega_{1,y}|^2\right) \qquad (42)$$

may open ways to infer these gradients[1].

10 Conclusion

We have performed an extensive study of the sensitivity of a combined ^{3}He/Cs magnetometer. We analyzed the performance of two different CsOPM modes of operation and found them to be identical in terms of magnetometric sensitivity. We have presented an expression which permits to predict the achievable sensitivity as a function of the signal frequency. The calculation is based on experimentally accessible parameters and thus provides a useful tool to judge the actual performance of a magnetometer system. The predictions were compared to measurements and an excellent agreement was found. Our results suggest that a deeper study of the laser power dependent effects in the ODMR process (power broadening of the magnetic resonance) might bring interesting insights, potentially leading to a selection criterion for Cs cells to be used in this application. The investigations of the PS-mode of operation suggest that a more elaborate driving scheme for the CsOPMs might lead to significantly improved sensitivity. We have estimated the expected sensitivity for the n2EDM geometry and found it to be compatible with the values reported in our experiments. Possible techniques to measure magnetic field gradients, which are a major source of systematic error in the n2EDM experiment, were discussed.

An additional option which is currently discussed is the installation of several small ^{3}He/Cs magnetometers inside the n2EDM apparatus. These magnetometers could be similar in design to the prototype described here and would yield measurements of the magnetic field at their respective position which could also be used to infer magnetic field gradients.

Author contribution statement

This work was made possible by the excellent support from the mechanical workshops of the Physics Department at the University of Fribourg and the University of Mainz. This work received financial support by grants from the Deutsche Forschungsgemeinschaft (HE2308/14-1) and the Swiss National Science Foundation (200020_140421). The studies presented in this paper are part of the Ph.D. thesis of H.-C. Koch who was leading all aspects of the investigations. The other authors contributed to particular subtasks as follows:

– A. Weis, Z.D. Grujić, P. Knowles, M. Kasprzak and W. Heil were involved in the conceptual planing and construction of the device and in the development of data acquisition methods.
– Z.D. Grujić, P.Knowles, G. Bison, A. Schnabel and J. Voigt contributed to the data taking at PTB.
– A. Weis, Z.D. Grujić, G. Bison and W. Heil participated in the data analysis and the discussion of the results.
– A. Kraft, A. Pazgalev, Z.D. Grujić, P.Knowles and M. Kasprzak contributed to important precursor measurements at Johannes Gutenberg University Mainz.

[1] Note that Cates et al. derived equation (42) for a spherical ^{3}He cell assuming only constant magnetic field gradients. See reference [20] for the definition of the variables.

References

1. C.A. Baker, G. Ban, K. Bodek, M. Burghoff, Z. Chowdhuri, M. Daum, M. Fertl, B. Franke, P. Geltenbort, K. Green, M.G.D. van der Grinten, E. Gutsmiedl, P.G. Harris, R. Henneck, P. Iaydjiev, S.N. Ivanov, N. Khomutov, M. Kasprzak, K. Kirch, S. Kistryn, S. Knappe-Güneberg, A. Knecht, P. Knowles, A. Kozela, B. Lauss, T. Lefort, Y. Lemière, O. Naviliat-Cuncic, J.M. Pendlebury, E. Pierre, F. M. Piegsa, G. Pignol, G. Quéméner, S. Roccia, P. Schmidt-Wellenburg, D. Shiers, K.F. Smith, A. Schnabel, L. Trahms, A. Weis, J. Zejma, J. Zenner, and G. Zsigmond, Phys. Proc. **17**, 159 (2011), 2nd International Workshop on the Physics of fundamental Symmetries and Interactions – PSI2010.
2. A. Riotto, M. Trodden, Ann. Rev. Nucl. Part. Sci. **49**, 35 (1999)
3. N.F. Ramsey, Phys. Rev. **76**, 996 (1949)
4. H.-C. Koch, G. Bison, Z.D. Grujić, W. Heil, M. Kasprzak, P. Knowles, A. Kraft, A. Pazgalev, A. Schnabel, J. Voigt, A. Weis, Eur. Phys. J. D **69**, 202 (2015)
5. J. Bork, H.D. Hahlbohm, R. Klein, A. Schnabel, in *Biomag2000, Proc. 12th Int. Conf. on Biomagnetism*, edited by J. Nenonen, R.J. Ilmoniemi, T. Katila (Helsinki University of Technology, Espoo, Finland, 2001), pp. 970–973
6. N. Castagna, G. Bison, G. Di Domenico, A. Hofer, P. Knowles, C. Macchione, H. Saudan, A. Weis, Appl. Phys. B **96**, 763 (2009)
7. S. Groeger, G. Bison, J.-L. Schenker, R. Wynands, A. Weis, Eur. Phys. J. D **38**, 239 (2006)
8. H.-C. Koch, Ph.D. thesis, Johannes Gutenberg-Universitaet Mainz (2015)
9. P. Knowles, G. Bison, N. Castagna, A. Hofer, A. Mtchedlishvili, A. Pazgalev, A. Weis, Nucl. Inst. Meth. A **611**, 306 (2009)
10. G. Bison, R. Wynands, A. Weis, Appl. Phys. B **76**, 325 (2003)
11. G. Bison, R. Wynands, A. Weis, J. Opt. Soc. Am. B **22**, 77 (2005)
12. R.C. Rao, Bull. Calcutta Math. Soc. **37**, 81 (1945)
13. H. Cramér, *Mathematical methods of statistics* (Princeton University Press, 1946)
14. D.C. Rife, R.R. Boorstyn, IEEE Trans. Inf. Theory **20**, 591 (1974)

15. C. Gemmel, W. Heil, S. Karpuk, K. Lenz, Ch. Ludwig, Yu. Sobolev, K. Tullney, M. Burghoff, W. Kilian, S. Knappe-Grüneberg, W. Müller, A. Schnabel, F. Seifert, L. Trahms, St. Baeßler, Eur. Phys. J. D **57**, 303 (2010)
16. D.B. Sullivan, D.W. Allan, D.A. Howe, F.L. Walls, *Characterization of clocks and oscillators* (National Institute of Standards and Technology, 1990)
17. I. Altarev, G. Ban, G. Bison, K. Bodek, M. Burghoff, M. Cvijovic, M. Daum, P. Fierlinger, E. Gutsmiedl, G. Hampel, W. Heil, R. Henneck, M. Horras, N. Khomutov, K. Kirch, St. Kistryn, S. Knappe-Grneberg, A. Knecht, P. Knowles, A. Kozela, J.V. Kratz, F. Kuchler, M. Kuniak, T. Lauer, B. Lauss, T. Lefort, A. Mtchedlishvili, O. Naviliat-Cuncic, S. Paul, A.S. Pazgalev, G. Petzoldt, E. Pierre, C. Plonka-Spehr, G. Qumner, D. Rebreyend, S. Roccia, G. Rogel, T. Sander-Thoemmes, A. Schnabel, N. Severijns, Yu. Sobolev, R. Stoepler, L. Trahms, A. Weis, N. Wiehl, J. Zejma, G. Zsigmond, Nucl. Instrum. Methods A **611**, 133 (2009)
18. S. Afach, C.A. Baker, G. Ban, G. Bison, K. Bodek, Z. Chowdhuri, M. Daum, M. Fertl, B. Franke, P. Geltenbort, K. Green, M.G.D. van der Grinten, Z. Grujic, P.G. Harris, W. Heil, V. Hélaine, R. Henneck, M. Horras, P. Iaydjiev, S.N. Ivanov, M. Kasprzak, Y. Kermaïdic, K. Kirch, P. Knowles, H.-C. Koch, S. Komposch, A. Kozela, J. Krempel, B. Lauss, T. Lefort, Y. Lemière, A. Mtchedlishvili, O. Naviliat-Cuncic, J.M. Pendlebury, F.M. Piegsa, G. Pignol, P.N. Prashant, G. Quéméner, D. Rebreyend, D. Ries, S. Roccia, P. Schmidt-Wellenburg, N. Severijns, A. Weis, E. Wursten, G. Wyszynski, J. Zejma, J. Zenner, G. Zsigmond, Eur. Phys. J. D **69**, 225 (2015)
19. A. Kraft, H.-C. Koch, M. Daum, W. Heil, Th. Lauer, D. Neumann, A. Pazgalev, Yu. Sobolev, A. Weis, Eur. Phys. J. Tech. Instrum. **1**, 1 (2014)
20. G.D. Cates, S.R. Schaefer, W. Happer, Phys. Rev. A **37**, 2877 (1988)